

Widely Tunable (2.47–2.64 μm) Hybrid Laser Based on GaSb/GaInAsSb Quantum-Wells and a Low-Loss Si_3N_4 Photonic Integrated Circuit

Samu-Pekka Ojanen,* Jukka Viheriälä, Nouman Zia, Eero Koivusalo, Joonas Hilska, Heidi Tuorila, and Mircea Guina

Photonic integrated circuits fabricated using a Si_3N_4 waveguide platform exhibit low losses in a wide wavelength region extending from visible to beyond 2 μm . This feature is exploited to demonstrate a high-performance integrated laser exhibiting broad wavelength tuneability near a 2.6 μm wavelength region. The laser is based on a Si_3N_4 photonic integrated circuit incorporating a tunable reflector and a AlGaInAsSb/GaSb quantum-well gain element. A tuning range of 170 nm (2474–2644 nm) and single-mode CW operation with a maximum power of 6.4 mW at room temperature are demonstrated. The performance is enabled by exploitation of several essential building blocks realized in Si_3N_4 , namely low-loss Y-branches, inverse tapers, and a double-ring resonator with a free spectral range of ≈ 160 nm. Moreover, the limits of wavelength coverage are explored using Si_3N_4 waveguides and show that the platform supports low propagation loss up to 3.5 μm . Finally, the possibility to achieve improved mode matching between Si_3N_4 and GaSb waveguides is analyzed, further enabling enhancing the performance of such a hybrid laser platform and supporting wavelength extension beyond a 3 μm range.

in volume-scalable photonics applications. Benefiting from the sustained long-term developments of silicon-photonics and InP integration platforms as well as a vigorous market pull, PIC technology is fairly well established for use in datacom operating at 1.3 and 1.55 μm wavelengths.^[1] On the other hand, to date there are virtually no other established commercial volume use-cases outside telecom arena although there are many other potential applications where PIC technology could prove disruptive, for example in LIDAR, sensing and biomedical technology. In particular, the 2–3 μm wavelength range has raised interest for sensing many important environmental and industrial gases, such as H_2S , C_2H_4 , CH_4 , CO , CO_2 , and N_2O ,^[2] and to measure biomarkers, such as lactate, urea, and glucose.^[3,4] Shorter wavelengths in the visible and <1.1 μm


1. Introduction

Photonic integration has been rapidly developing owing to many benefits inherent to fabrication and use of miniaturized on-chip photonic systems. Photonic integrated circuits (PICs) enable lower cost and volume manufacturing, fostering a wider adoption

near-infrared (NIR) region are also relevant in life science and health-related applications, for example in optical coherence tomography^[5] and biochemical sensing.^[6–8] All these point to the need to develop multispectral PICs, starting with the availability of PIC-compatible light sources that can be integrated with silicon photonics or Si_3N_4 platforms.

To this end, Si_3N_4 waveguide technology has been widely recognized as a wavelength-agnostic integration platform^[9] supporting broadband operation from visible to beyond 2 μm ,^[10] thus making it an attractive solution for multi-spectral sensing. Moreover, Si_3N_4 -based PICs and their chip design tools^[11] are commoditized to a mature level using external foundries. However, availability of the integrated light sources is severely limiting the applicability of Si_3N_4 -PICs toward sensing applications. As a matter of fact, to the best of our knowledge, so far all integrated light sources emitting near 2 μm wavelength utilize silicon-on-insulator (SOI) platforms.^[12,13] Moreover, the technical readiness of the light sources integrated with SOI at this wavelength band is relatively poor with just a few demonstrations, largely based on InP type-II quantum wells (QWs),^[13,14] limited in terms of spectral coverage to < 2.4 μm . We should also note that SOI-waveguides are not transparent at wavelengths below 1.1 μm , therefore rendering it impossible to combine visible domain sensing functions with mid-IR.

S.-P. Ojanen, J. Viheriälä, N. Zia, E. Koivusalo, J. Hilska, H. Tuorila, M. Guina
Optoelectronics Research Centre
Photonics Laboratory
Physics Unit
Faculty of Engineering and Natural Sciences
Tampere University
Korkeakoulunkatu 3, Tampere 33720, Finland
E-mail: samu-pekka.ojanen@tuni.fi

 The ORCID identification number(s) for the author(s) of this article can be found under <https://doi.org/10.1002/lpor.202201028>

© 2023 The Authors. Laser & Photonics Reviews published by Wiley-VCH GmbH. This is an open access article under the terms of the Creative Commons Attribution-NonCommercial-NoDerivs License, which permits use and distribution in any medium, provided the original work is properly cited, the use is non-commercial and no modifications or adaptations are made.

DOI: 10.1002/lpor.202201028

At wavelengths beyond 2.5 μm , SiO_2 starts to exhibit losses,^[15] which makes commonly used 220 nm SOI-waveguides relatively lossy due to enhanced SiO_2 -cladding interaction at long wavelengths. This can be circumvented by utilizing thick $\text{Si}^{[16]}$ or Si_3N_4 waveguides to minimize light interaction with SiO_2 -cladding, or by approaches based on Ge-on-Si waveguides^[17] or suspended Si-waveguides,^[18] which alleviate SiO_2 claddings loss. However, the maturity of these alternative approaches is lower compared with Si_3N_4 or SOI PICs. The advantage of these alternative methods is more evident for wavelengths beyond 4 μm where SiO_2 loss increases more than one order of magnitude. In contrast to the SOI platform, Si_3N_4 waveguides cladded by SiO_2 have relatively low index contrast, which makes them less prone to waveguide scattering, enabling much lower propagation loss values compared to SOI platforms. Low index contrast also makes Si_3N_4 waveguides less sensitive to width and index variation, making it easier to manufacture wavelength insensitive structures. This is attractive for sensing applications, where specific narrow absorption regions need to be targeted. On the other hand, Si_3N_4 has lower thermo-optical coefficient compared to silicon, increasing the size and power consumption of thermal phase control elements.^[19] Recently, these features have been exploited at telecom wavelengths to realize a broad tuning range Si_3N_4 hybrid external cavity laser (ECL).^[20]

In terms of integration choices, we would note that although heterogeneous integration has been developed to combine III–V materials with Si_3N_4 waveguides,^[21,22] hybrid integration is more mature allowing integration of PIC chips available from foundries.^[23] Moreover, higher performance is expected for emerging III–V/ Si_3N_4 hybrid lasers since the gain chips and passive chips can be individually optimized and tested before integration. Furthermore, thermal management is also easier for chips placed separately on different carriers.

When it comes to possibility to achieve light emission in the whole 2–3 μm wavelength range, GaSb-based optoelectronics platform is attractive for PIC integration, ensuring high gain at relatively low thresholds and low operation voltage. In fact, AlGaInAsSb/GaSb-based type-I laser diodes can reach an emission wavelength of up to 3.7 μm ,^[24] while the alternative InP-based material system is limited in wavelength coverage to ≈ 2.3 –2.4 μm using type-II QW interband transitions.^[13,14] Hybrid GaSb/SOI lasers circuitry has been already demonstrated near 2 μm , targeting wavelength-tailoring^[12] and laser stabilization.^[25] Moreover, recently we have demonstrated a tunable GaSb/SOI hybrid laser at 2.5–2.6 μm window,^[26] yet the power performance was somewhat impaired by high losses associated with passive SOI circuitry. We should also note that when moving from the 2 μm region toward 3 μm , the Auger recombination current and carrier confinement and transport in AlGaInAsSb materials lead to the relatively rapid increase of temperature sensitivity and thermal roll-over. Therefore, achieving lower waveguide losses, and hence lower threshold currents, is becoming significantly more critical when operating beyond 2.5 μm . In this paper, we tackle this issue by utilizing low-loss and high precision 800-nm-thick Si_3N_4 waveguides fabricated using LIGENTECH open-access foundry services,^[27] leading to significant performance improvement compared to previous SOI-based demonstration. In particular, we demonstrate a GaSb/ Si_3N_4 -PIC hybrid laser, which outperforms in tuning range and in power also the con-

ventional ECLs using the Littrow configuration demonstrated with the similar gain material^[26]; we demonstrate record wavelength tunability (> 170 nm) ≈ 2.4 –2.6 μm hybrid laser with mW-level output power across the tuning range, which is an attractive source for various multi-wavelength spectroscopy applications. Besides offering a significantly more compact footprint compared to SOI platform, our demonstration proves the advantages of using Si_3N_4 waveguide technology for the development of high-performance lasers for PIC-based applications at 2–3 μm .

Figure 1 shows a schematic of the GaSb/ Si_3N_4 hybrid laser with wide wavelength-tunability demonstrated in this work. The coupling between GaSb and Si_3N_4 is optimized using active alignment between two different chips, which enables an easier study on the optimization of coupling losses. Yet, in terms of moving toward on-chip integration and more complex PIC functionality, we also note the first demonstration of flip-chip integration of GaSb gain elements on SOI circuits operating at 2 μm region.^[28] Detailed design and fabrication consideration are provided in the next subsections.

2. GaSb Gain Chip Technology

To generate light in the 2–3 μm wavelength region, a GaSb-based type-I QW structure was utilized. The epitaxial structure consisted of two compressively strained $\text{Ga}_{0.54}\text{In}_{0.46}\text{As}_{0.13}\text{Sb}_{0.87}$ QWs, with 1.9% strain and an $\text{Al}_{0.25}\text{Ga}_{0.75}\text{As}_{0.02}\text{Sb}_{0.98}$ barrier in between. The QWs were positioned between two 270-nm-thick lattice-matched $\text{Al}_{0.25}\text{Ga}_{0.75}\text{As}_{0.02}\text{Sb}_{0.98}$ waveguide layers, which were embedded between 2- μm -thick p- and n-doped $\text{Al}_{0.60}\text{Ga}_{0.40}\text{As}_{0.05}\text{Sb}_{0.95}$ cladding layers. The alloy compositions given here are values from high-resolution X-ray diffraction measurements and corresponding simulations based on the dynamical diffraction theory.^[29] The doping levels in the cladding were graded close to the waveguide layers to minimize free carrier absorption near the active region.

A 2000 μm long and 450 μm wide RSOA chip was manufactured to provide gain and cavity feedback in the laser circuit. The RSOA chip employed a single-mode ridge waveguide (RWG) with a 5 μm width and a “J-shaped” structure, where the RWG has a bent waveguide with a 7° output angle at the front facet to minimize back reflections, and an AR coating to maximize out-coupled light. The RWG bend follows an Euler spiral geometry,^[30] where the curvature increases linearly along the bend. The minimum bend radius was 18 mm, leading to negligible bending losses. The rear facet of the RSOA had a straight waveguide, and was left as-cleaved, leading to $\approx 30\%$ reflectance. A schematic of the RSOA is shown in **Figure 2**.

The RSOA was mounted p-side down on an AlN submount to improve the dissipation of active region temperature for maximum efficiency. The AlN submount was placed on a copper heatsink for characterization, and thermally stabilized at room temperature (23 °C). Pulsed current with 100 kHz frequency and 10% duty cycle was injected into the RSOA to minimize heating effects. The average amplified spontaneous emission (ASE) output power was measured from the front facet as a function of the injection current, and this is shown in **Figure 3a**.

The ASE spectrum shown in **Figure 3b** was measured at a constant current of 600 mA, coupling the output of the RSOA to a multi-mode (MM) fiber, and using a Fourier transform infrared

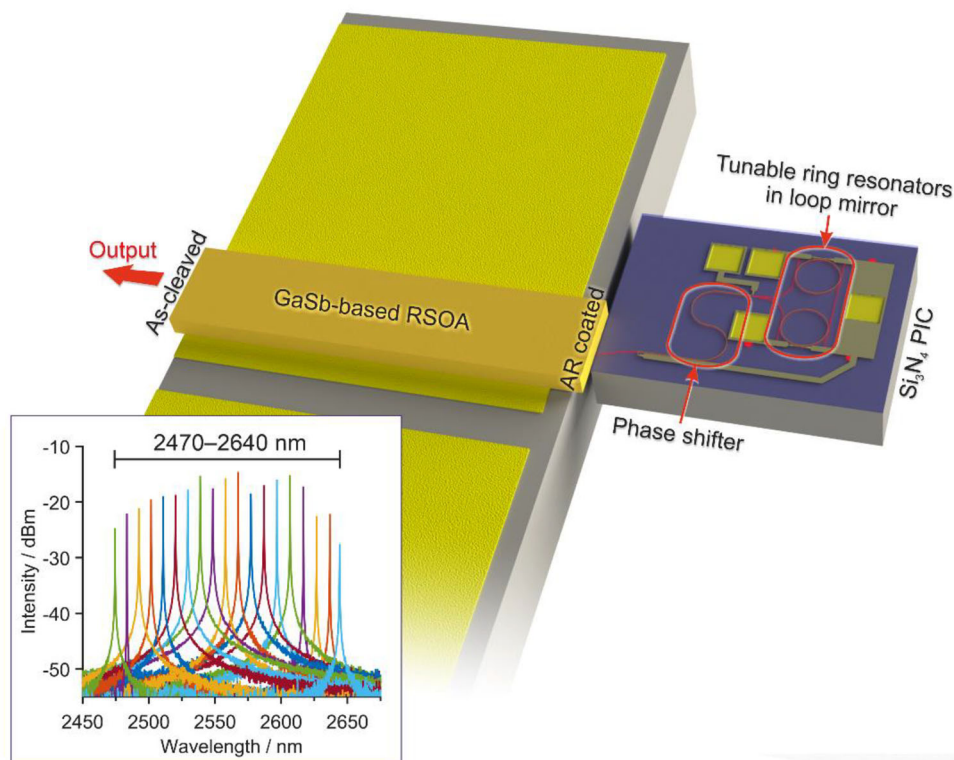


Figure 1. Schematic of the GaSb/Si₃N₄ hybrid laser with a wide wavelength-tunability demonstrated in this work. The hybrid laser consists of a GaSb-based reflective semiconductor optical amplifier (RSOA) to provide gain in the 2.47–2.64 μm wavelength region. The RSOA is bonded p-side down on an AlN submount, and edge-coupled to a Si₃N₄ PIC, which consists of a resistively tunable double-ring resonator in a loop mirror configuration for filtering and tuning the wavelength. The circuit has a phase shifter to allow phase-matching the PIC with the RSOA. The RSOA and PIC facets have anti-reflectance (AR) coatings to minimize parasitic reflections and maximize transmission.

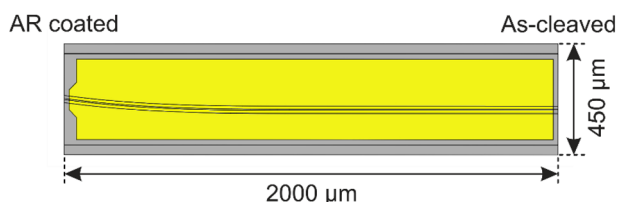


Figure 2. Schematic of the RSOA chip.

(FTIR) spectrometer. Looking at the spectrum, the maximum intensity is at $\approx 2.55 \mu\text{m}$, and the full-width half maximum (FWHM) is 97 nm.

3. Assessment of Losses Beyond 2.5 μm in Si₃N₄ Waveguides

To explore the feasibility of using Si₃N₄ waveguide beyond 2.5 μm wavelength band we studied how SiO₂-cladding absorption contributes to the Si₃N₄ waveguide propagation. To this end we used Ansys Lumerical Finite Difference Eigenmode (FDE) solver. Here we utilized SiO₂ absorption values from the literature, which also indicate that below 2.5 μm contribution of SiO₂ absorption to losses is minimal.^[15] The absorption loss was simulated for the widest single-mode (SM) waveguide, which supports only the fundamental mode, as well as for a MM waveguide, which was

set to be 2 μm wider than the SM waveguide. The SiO₂ absorption loss as a function of wavelength for SM and MM waveguides is shown in **Figure 4**. The absorption loss of the MM waveguide is smaller than the SM waveguide due to higher lateral mode confinement. The absorption loss stays below 1 dB cm⁻¹ at wavelengths shorter than 2.7 μm and reaches a peak of 2.4 and 1.7 dB cm⁻¹ at 2.9 μm, for the SM and MM waveguides, respectively. The losses then decrease rapidly and are below 0.5 dB cm⁻¹ for both the SM and MM waveguides in the 3.1–3.4 μm wavelength region. Then they start to again rise rapidly, reaching a maximum of 3.5 and 3.0 dB cm⁻¹ at 4 μm, for the SM and MM waveguides, respectively. The most optimum regions for 800-nm-thick Si₃N₄ waveguides in terms of losses are thus clearly 2.4–2.7 μm and 3.1–3.4 μm. While the losses are much higher at other wavelengths, they are still small enough for most hybrid laser configurations. It should be noted that the actual losses are somewhat higher due to scattering from the waveguide edges.^[31]

In this paper we target the 2.4–2.7 μm wavelength region, where SiO₂ absorption loss is still low, and gases like H₂O and CO₂ exhibit strong absorption peaks. To prevent the excitation of higher-order modes in this wavelength region, a waveguide width of 1.65 μm was chosen, which is the widest waveguide where single-mode operation is maintained over the 2.4–2.7 μm wavelength region. The shape of the mode was simulated with Ansys Lumerical FDE solver is shown in **Figure 5a**. The propagation loss of the 1.65 μm × 0.8 μm waveguide was measured using the

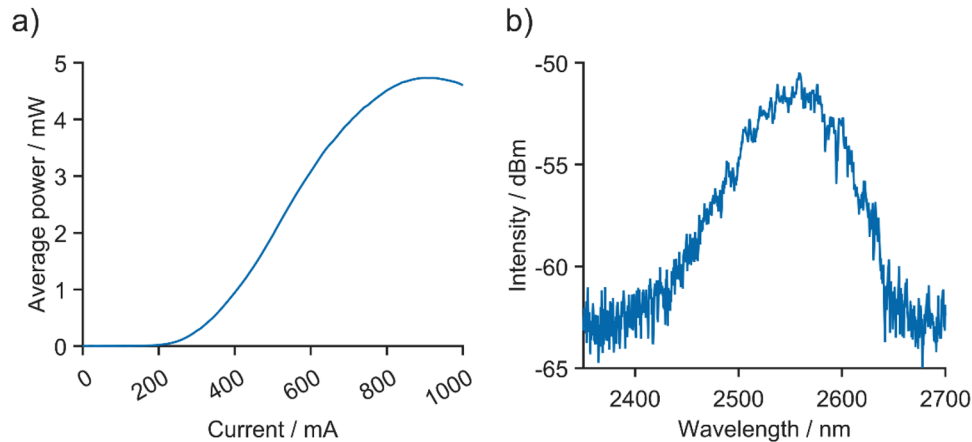


Figure 3. a) The ASE average power of the RSOA as a function of injection current at room temperature, and b) the ASE spectrum of the RSOA at 600 mA injection current.

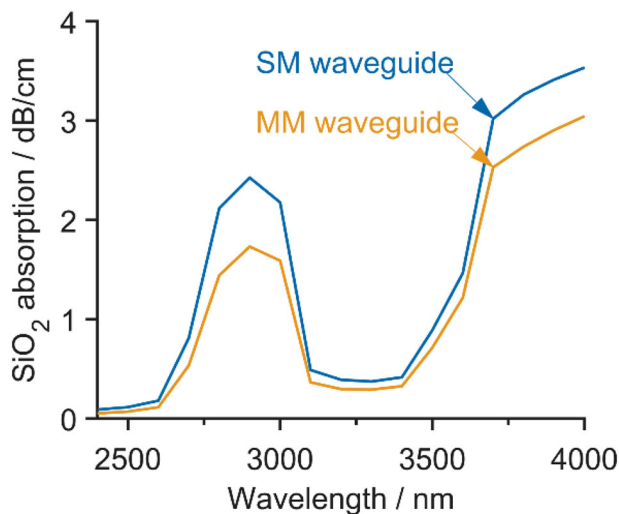


Figure 4. SiO₂ cladding absorption loss as a function of wavelength for an SM waveguide, and an MM waveguide.

cut-back method, where a series of three spirals with a waveguide bend radius of 50 μm was manufactured, and the loss of these spirals was measured with respect to a straight waveguide. The loss values were measured using a Norcada DFB laser at 2.68 μm wavelength designed for CO₂ spectroscopy. The waveguide loss as a function of spiral length is shown in Figure 5b. Fitting a slope yields a waveguide propagation loss of 0.67 dB cm⁻¹ at 2.68 μm , which is close to the absorption loss given by the simulation (0.71 dB cm⁻¹). Since the measured 0.67 dB cm⁻¹ also includes the scattering losses, the actual SiO₂-cladding absorption is most likely smaller than what is given in the literature.^[15] The y-axis intersection of the linear fit is 1.407 dB, which corresponds to a 0.017 dB bend loss at 2.68 μm .

4. Tunable Reflector and Extended Cavity Design

Figure 6 shows a schematic of the Si₃N₄ circuit that was utilized as a wavelength filtering and tuning element in the hybrid laser

cavity. The circuit consists of an AR-coated input waveguide with an inverse taper at the coupling facet, a phase shifter, and a Y-branch, which was used to form a loop mirror on the PIC. Two tunable micro-ring resonators (MRRs) were placed inside the loop mirror to form a single-pass Vernier reflector. Archimedean spirals were placed at the through ports of each ring resonator to suppress reflections. The waveguide bends on the PIC utilized a bend radius of 100 μm , leading to negligible loss. The inverse taper was placed at a 17-degree angle with respect to the PIC facet to match the output angle of the RSOA to maximize the coupling efficiency.

4.1. Inverse Taper Design and Loss

One of the most critical parts in hybrid integration is the coupling efficiency between the RSOA and Si₃N₄ waveguide. The coupling loss can be effectively suppressed by mode matching between the two edge-coupled waveguides. There exist various approaches for edge-coupling light efficiently between RSOA and Si₃N₄ waveguides, including an inverse taper, where the Si₃N₄ waveguide width is tapered toward the facet to minimize mode mismatch,^[28] photonic wire bonds,^[32] or by printing beam-shaping elements to the facets.^[33] The inverse taper is the simplest approach out of these, as it is patterned in the same lithography step as the Si₃N₄ waveguide and does not require any backend processing.

A schematic of the coupling interface between RSOA and a Si₃N₄ PIC with an inverse taper is shown in **Figure 7**, together with the fundamental transverse electric (TE) modes of the RSOA waveguide, the Si₃N₄ waveguide at the taper input, and the Si₃N₄ waveguide at the taper output. The coupling loss between the RSOA waveguide, and the Si₃N₄ waveguide is determined by the air gap size, as well as the geometry of the taper, i.e., its width and its length.

To optimize the taper input width, simulations were performed with Ansys Lumerical FDE solver. The mode mismatch loss between the RSOA mode and the mode at the Si₃N₄ taper input was simulated by fixing the RSOA geometry and varying the Si₃N₄ taper input width. The mode mismatch loss as a function of taper width is shown in **Figure 8a**. A minimum mode mismatch

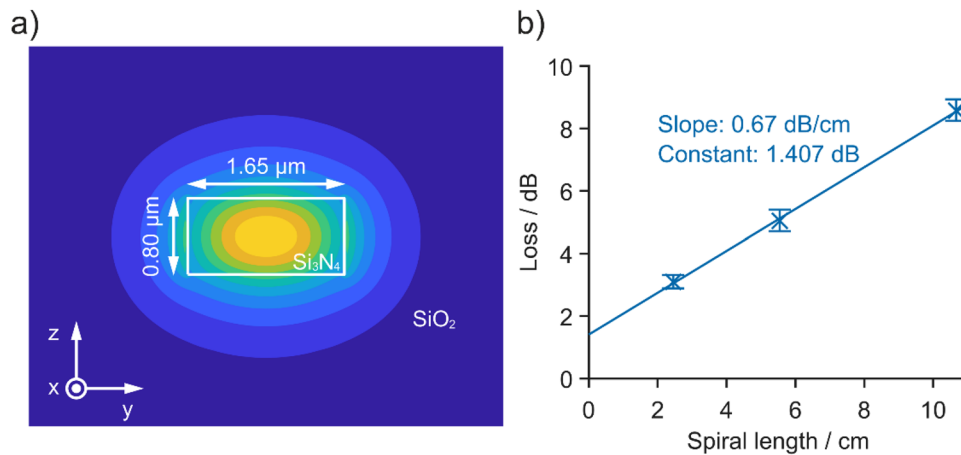


Figure 5. a) The 2D fundamental TE mode of the Si_3N_4 $1.65 \mu\text{m} \times 0.8 \mu\text{m}$ waveguide, and b) the loss of the waveguide spiral with respect to a straight waveguide, as a function of spiral length.

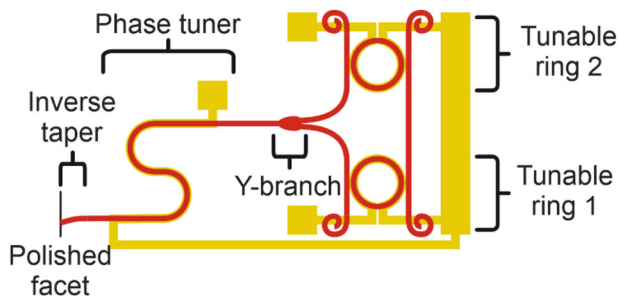


Figure 6. Schematic of the Si_3N_4 circuit. The red lines represent waveguides, and the yellow regions represent resistive heaters.

loss of ≈ 0.75 dB is obtained for $0.65 \mu\text{m}$ wide taper input width. While the $0.65 \mu\text{m}$ is the optimum width according to the simulation, a $0.4 \mu\text{m}$ taper input width was used in the Si_3N_4 circuit in this work. This value was optimized for $2.65 \mu\text{m}$ wavelength and a different RSOA epitaxial structure, which did not perform sufficiently well in the hybrid laser experiment. This leads to a higher mode mismatch loss of ≈ 1.6 dB at $2.55 \mu\text{m}$ wavelength between the RSOA and the Si_3N_4 circuit that are used in this work.

To estimate the effect of the air gap size between the RSOA and Si_3N_4 waveguides on the coupling loss, simulations were performed using an Ansys Lumerical FDTD solver. The taper input width was set to $0.4 \mu\text{m}$ to match the actual inverse taper utilized in the Si_3N_4 circuit, and the air gap was swept, and the transmission was extracted. The effect of AR coatings was also considered. The simulated coupling loss as a function of the air gap is shown in Figure 8b. The coupling loss is robust, staying below 2 dB up to $1.5 \mu\text{m}$ air gap size.

Figure 9a shows a schematic of the circuit that was used to measure the coupling efficiency. The PIC had a $50 \mu\text{m}$ long inverse taper at the input waveguide, tapering from $0.4 \mu\text{m}$ up to $1.65 \mu\text{m}$, a 90° bend with a $200 \mu\text{m}$ bend radius, leading to a negligible bend loss, and an output waveguide to the side of the PIC. Having the output at the side minimizes the signal that does not couple to the waveguide from reaching the detector. The input and output waveguides were AR coated to minimize inser-

tion loss and reflections and to get as accurate value for the coupling loss as possible. The straight waveguide side of a p-side up mounted J-bend RSOA was coupled to the PIC and the output signal from the PIC was measured with an integrating sphere and a photodetector. The output from the RSOA was first measured at a fixed injection current value of 800 mA with an integrating sphere and a VIGO HgCdTe four-stage thermoelectrically cooled PVI-4TE photodetector. Then the PIC was placed as close to the RSOA as allowed by the setup, and the horizontal and vertical positions were optimized with closed-loop piezo drivers, while monitoring the output signal from the PIC. The gap between the RSOA and PIC was then gradually increased, optimizing the horizontal and vertical positions at each point. The coupling efficiency at each gap size was obtained by dividing the output from the PIC by the output from the RSOA. The background noise of the PIC output was subtracted at each point. Figure 9b shows the coupling loss as a function of distance from the reference. A minimum coupling loss of ≈ 2.9 dB was measured at the minimum distance. Based on the simulation (Figure 8b), 2.9 dB loss corresponds to an air gap size of $\approx 3.5 \mu\text{m}$, which seems a realistic value if compared to the simulation.

4.2. Photonics Inverse Design of a Low-Loss Y-Branch

A Y-branch, which couples light from one input channel equally into two output channels, was utilized to form the loop mirror in the Si_3N_4 circuit. We designed a low-loss Y-branch with $1.65 \mu\text{m} \times 0.8 \mu\text{m}$ input and output channels and a small footprint of $8.65 \mu\text{m} \times 29 \mu\text{m}$, utilizing an Ansys Lumerical Photonic Inverse Design (PID) package. Here a parametrized geometry was defined, and its shape was optimized by using the adjoint method and gradient descent^[34] minimizing the insertion loss. A rectangular Y-branch shape was used as an initial guess. The final optimized shape is shown in Figure 10a. A loss of 0.05 dB across the $2.5\text{--}2.7 \mu\text{m}$ wavelength band was obtained from the simulation. To measure the loss of the optimized Y-branch structure, a series of 30 and 58 Y-branches was manufactured, and their loss was measured with respect to a straight waveguide. The loss as a

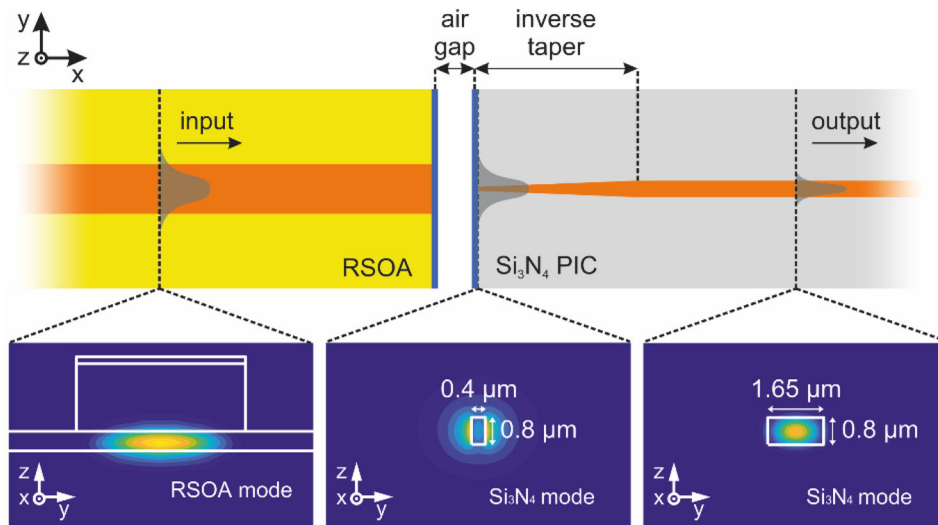


Figure 7. Schematic of the RSOA and Si_3N_4 PIC coupling interface, and the simulated 2D fundamental TE mode profiles of the RSOA waveguide, the Si_3N_4 waveguide at the taper input ($0.4 \times 0.8 \mu\text{m}$), and the Si_3N_4 waveguide at the taper output ($1.65 \times 0.8 \mu\text{m}$).

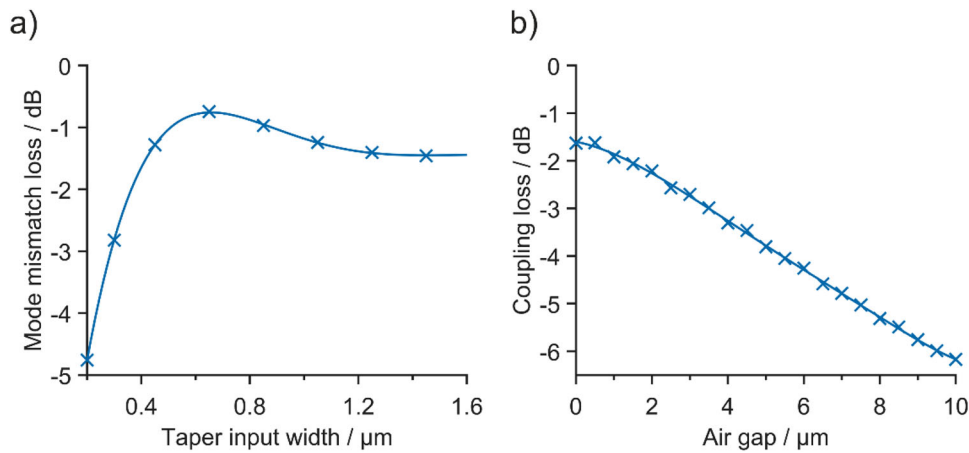


Figure 8. a) Simulated coupling loss as a function of Si_3N_4 waveguide width, and b) the simulated coupling loss as a function of air gap for a Si_3N_4 waveguide width of $0.4 \mu\text{m}$.

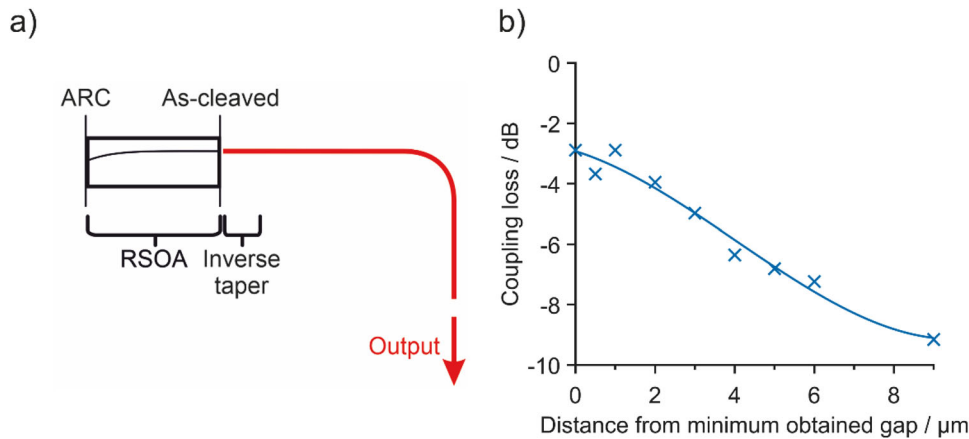


Figure 9. a) The schematic of the coupling efficiency measurement circuit. The red line represents the Si_3N_4 waveguide. b) The coupling efficiency as a function of distance from a reference point corresponding to the smallest gap between the RSOA and the PIC.

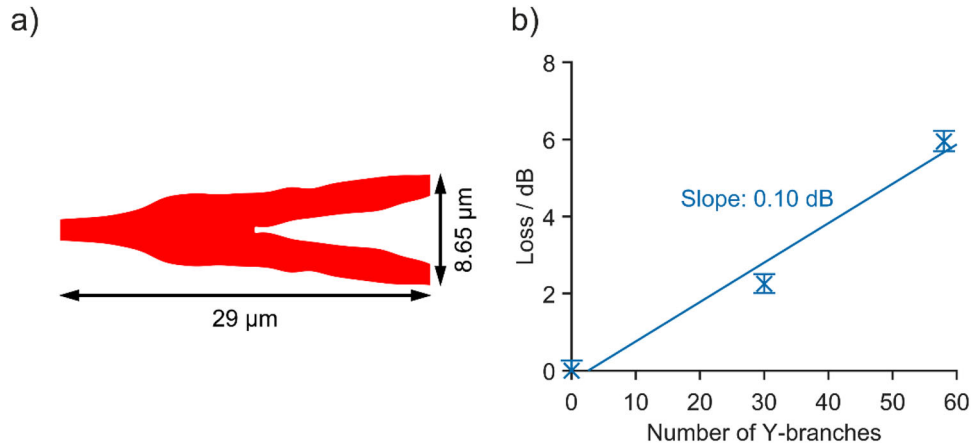


Figure 10. a) The optimized Y-branch structure, and b) the insertion loss as a function of the number of Y-branches.

function of the number of Y-branches is shown in Figure 10b. By making a linear fit to the measurement points, an insertion loss of 0.10 dB at 2.68 μm was measured for the optimized Y-branch structure, which is close to the simulated value.

4.3. Double-Ring Resonator Vernier Filter Design

Tunable MRRs were used to achieve wavelength tuning in the hybrid laser. The free spectral range (FSR) of a single MRR is given by^[35]

$$\Delta\lambda_{MRR} = \frac{\lambda^2}{n_g L_{MRR}} \quad (1)$$

where λ is the central wavelength, n_g is the group index of the MRR waveguide, and L_{MRR} is the roundtrip length of the MRR. The MRR resonance wavelengths can be tuned by changing the group index. In this work, this was achieved by placing a resistively tuned heater on top of the MRR waveguide. Injecting current into the heater will heat the waveguide, which leads to a change in the refractive index of the Si_3N_4 waveguide through the thermo-optic effect. This changes the group index of the Si_3N_4 waveguide mode, changing its phase. The response time of the resistive heater, i.e. the time it takes for the waveguide to reach its equilibrium temperature after the current injected to the heater is changed, is in 10-kHz range^[23].

The suggested maximum temperature for the heater is 400 $^\circ\text{C}$, which limits the amount of current that can be injected into the heater. Thermal simulations were performed to determine what is the maximum phase shift that can be achieved in the waveguide, which depends on its length. To be able to tune the heater over one FSR of the MRR, a 2π phase shift is required. Thermal simulations were performed with COMSOL Multiphysics' Heat Transfer in Solids to determine how much the temperature of the waveguide below the heater changes when the heater is at its maximum temperature. The simulations indicate that the waveguide reaches a 250 $^\circ\text{C}$ temperature. Since the thermo-optic coefficient of Si_3N_4 is $2.43 \times 10^{-5} \text{ K}^{-1}$ and the effective index of the waveguide mode is ≈ 1.96 , the minimum waveguide length to achieve 2π phase shift in the waveguide can be calculated to be

$\approx 580 \mu\text{m}$. This leads to a minimum MRR radius of $\approx 100 \mu\text{m}$. A bend waveguide with a 100 μm radius was simulated with Ansys Lumerical FDE, and group indices of 2.11 and 2.08 were obtained at 2.6 and 2.5 μm , respectively. Plugging these into Equation (1) gives FSR values of 5.10 and 4.78 nm at these wavelengths.

To achieve stable single-mode operation of the hybrid laser, the FSR of the MRR should be broad enough compared to the gain spectrum of the RSOA. This is to restrict the feedback from the ring resonator to a single wavelength. Here the ASE emission spectrum of the RSOA had a wide FWHM of $\approx 100 \text{ nm}$ (see Figure 3 b), while the maximum FSR of the MRR is in the order of 5 nm, which means a single MRR is not enough to achieve longitudinal single-mode operation. To extend the FSR, two MRRs with slightly different radii were utilized, which leads to the Vernier effect. The FSR of this kind of Vernier filter is.^[36]

$$\Delta\lambda_V = M_{MRR1} \Delta\lambda_{MRR1} = M_{MRR2} \Delta\lambda_{MRR2}, \quad (2)$$

where $\Delta\lambda_{MRR1}$ and $\Delta\lambda_{MRR2}$ are the FSRs of the two MRRs, and M_{MRR1} and M_{MRR2} are coprime integers. By substituting Equation (1) to Equation (2), one obtains a relationship between the radii of the MRRs, R_{MRR1} and R_{MRR2} :

$$R_{MRR2} = \frac{M_{MRR2}}{M_{MRR1}} R_{MRR1}. \quad (3)$$

To investigate the limit of wavelength tuning, a target FSR of 160 nm was chosen. A suitable FSR can be achieved by choosing $M_{MRR2} = 33$ and $M_{MRR1} = 32$. By selecting $R_{MRR1} = 100 \mu\text{m}$ for the radius of one of the MRRs, one then obtains $R_{MRR2} = 103.125 \mu\text{m}$ for the radius of the other MRR by utilizing Equation (3). In this case, the estimated FSR of the Vernier filter will be 163 nm at 2.6 μm and 153 nm at 2.5 μm . A coupling gap of 650 nm was chosen for the MRRs, to get sufficient contrast between the maximum Vernier transmission peak and the side peaks adjacent to it, so that single-mode lasing is achieved, while keeping the losses within a reasonable range.

The building blocks of the MRRs, i.e., the directional coupler and the waveguide bend were simulated using Ansys Lumerical FDE and FDTD, assuming 0.67 dB cm^{-1} waveguide loss, and the transmission of the Vernier filter was simulated using Ansys

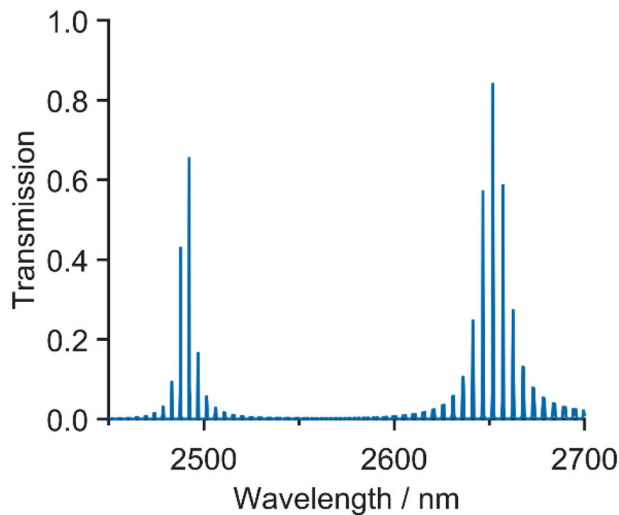


Figure 11. The transmission of the Vernier filter as a function of wavelength.

Lumerical INTERCONNECT. The transmission as a function of wavelength is shown in **Figure 11**. Based on the simulation, the FSR of the Vernier filter is 160 nm, which is close to the target. The loss of the Vernier filter is ≈ 0.75 dB at 2651 nm and 1.21 dB at 2492 nm. The increased loss and higher contrast between central and side peaks at shorter wavelengths are due to higher mode confinement, leading to a smaller coupling constant in the directional coupler of the MRRs.

4.4. Modes and Phase-Matching of the Hybrid Laser

The modes of the hybrid laser cavity depend on the phase of the Si_3N_4 circuit. The modes of the cavity can be calculated by solving the following equation for different values of the integer m ^[37]:

$$2\beta_{\text{RSOA}}L_{\text{RSOA}} - \phi_{\text{eff}} = 2\pi m, \quad (4)$$

where β_{RSOA} is the propagation constant of the RSOA, L_{RSOA} is the length of the RSOA, and ϕ_{eff} is the phase-shift induced by the external part of the cavity, which comprises of the bend waveguide facet of the RSOA, the input facet of the Si_3N_4 circuit, the coupling gap between these two, as well as all the building blocks of the Si_3N_4 circuit. To tune the external phaseshift ϕ_{eff} , a phase shifter was included in the Si_3N_4 waveguide. The phase shifter comprised of a resistively tuned heater placed above the Si_3N_4 waveguide. To be able to optimize ϕ_{eff} for maximum phase-match between the RSOA and the Si_3N_4 circuit, a 2π phase shift is required, and as mentioned earlier in Section 4.1, the shortest waveguide to achieve this without damaging the heater is ≈ 580 μm . The length of the phase shifter was thus set to 700 μm to ensure that the heater is not damaged during phase tuning.

To analyze the sensitivity of the external phase shift ϕ_{eff} to the PIC reflectance, first the external reflection coefficient r_{ext} , which includes the RSOA front facet, coupling gap, Si_3N_4 waveguide facet, and the Si_3N_4 building blocks, was simulated with Ansys Lumerical INTERCONNECT. The building block losses were assumed to be equal to the measured values. The external reflection

coefficient r_{ext} is related to the external phase shift ϕ_{eff} by the following equation:^[37]

$$r_{\text{ext}} = |r_{\text{ext}}| e^{i\phi_{\text{eff}}}. \quad (5)$$

According to Equation (5), the external reflectance is then $|r_{\text{ext}}|^2$. The MRRs were tuned so that there is a maximum reflectance of ≈ 2585 nm, which is close to the gain maximum. The simulated external reflectance $|r_{\text{ext}}|^2$ as a function of wavelength is shown in **Figure 12a**. The external reflectance is much lower than the simulated Vernier transmission, which is mostly due to the 3 dB coupling loss, leading to a 6 dB roundtrip loss. The cavity modes were next calculated as a function of the phase shift induced by the phase shifter, by plugging the simulated ϕ_{eff} into Equation (4), and assuming that there is no phase noise. The reflectance of the hybrid laser cavity mode exhibiting the highest reflectance was taken at each phase shift value, and this was plotted as a function of the phase shift induced by the phase shifter. The result is shown in **Figure 12b**. As can be seen from the figure, the maximum reflectance from the PIC depends strongly on the phase shift. Strong reflectance of 0.19 is achieved at 0.6π phase shift, which corresponds to the case where there is a lasing mode close to the wavelength where the external reflectance has its maximum value, i.e., the Si_3N_4 circuit and RSOA are perfectly phase-matched. Far away from 0.6π phase shift value, the reflectance is much lower, reaching values as low as ≈ 0.01 . These low reflectance regions correspond to the case where there is no lasing mode at the wavelength where the external reflectance has its maximum value, i.e., the Si_3N_4 circuit and RSOA are not phase-matched. This clearly shows the importance of having a phase shifter, which allows phase-matching the RSOA with the Si_3N_4 circuit to maximize the reflectance and thus the spectral purity of the hybrid laser.

5. Laser Performance

The schematic of the hybrid laser was illustrated earlier in **Figure 1**. The front facet of the RSOA on the AlN submount was coupled to the input waveguide of the Si_3N_4 PIC, and the output of the hybrid laser was located at the rear facet of the RSOA. By having the output at the rear facet of the RSOA, as opposed to having an output channel on the PIC, the output power is not as sensitive to Si_3N_4 PIC building block losses and coupling losses, allowing much higher output powers to be achieved.

To characterize the hybrid laser, the RSOA on AlN submount was placed on a heatsink, which was stabilized to room temperature. Moreover, the Si_3N_4 PIC was placed on a 3-axis closed-loop piezo stage. Continuous wave (CW) current was injected into the RSOA with probe needles, and the output of the hybrid laser was coupled to a MM fiber. The signal magnitude was measured with a photodiode. The RSOA and PIC were brought manually as close to each other as possible, and the waveguides were aligned by using the piezo stage to scan the vertical (z) and horizontal directions (y) and finding the position that has the maximum signal. **Figure 13** shows a 2D plot of a piezo scan done near the optimum position, with x axis showing the horizontal (y) position, y axis showing the vertical (z) position, and the color indicating the relative intensity of the signal measured with the photodiode, with

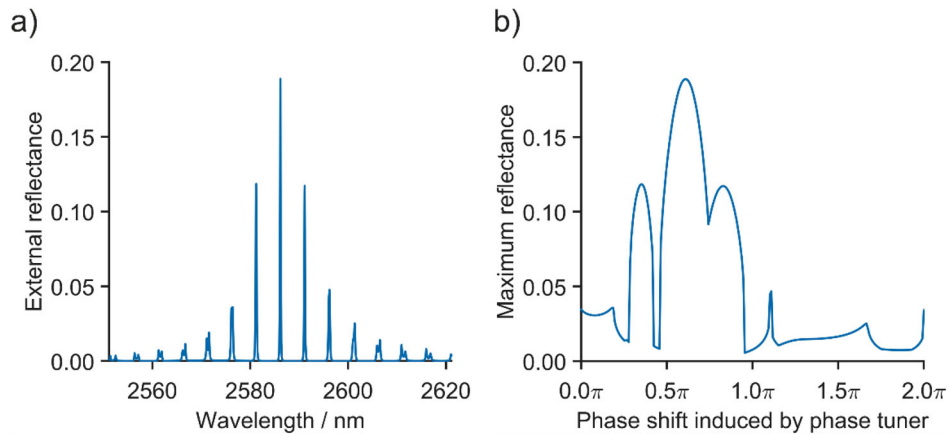


Figure 12. a) External reflectance as a function of wavelength, and b) the maximum reflectance as a function of the phase shift induced by the phase shifter.

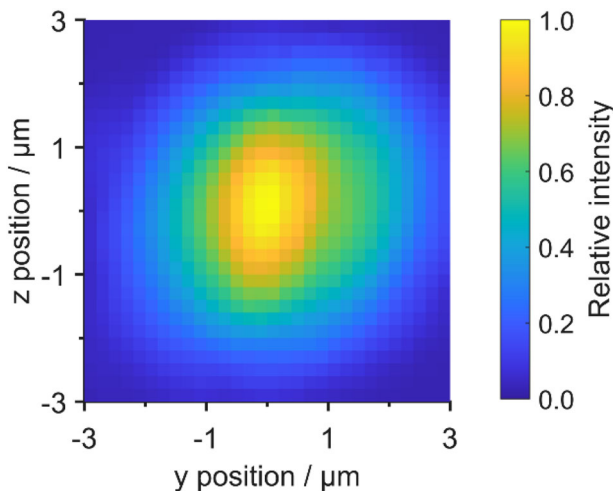


Figure 13. 2D plot of a 2D piezo scan of the PIC along the y and z axes. X and y axes of the plot show the y and z position, respectively. The color indicates the relative intensity of the signal measured with the photodiode, with 1.0 corresponding to the maximum signal.

1.0 corresponding to the maximum signal. As can be seen from the figure, proper alignment of the waveguides requires sub-μm alignment accuracy.

After the optimum alignment was achieved, the current was injected into one of the heaters attached to the MRRs to tune the emission wavelength of the hybrid laser to 2.55 μm, which is close to the point where the RSOA exhibits maximum gain. The light-current (LI) curve of the hybrid laser was then measured from 0 to 400 mA. The result is shown in blue in **Figure 14**. The hybrid laser has a threshold current of 190 mA and reaches a maximum CW output power of 6.4 mW for 322 mA. This is the highest CW output power measured from a hybrid laser at this wavelength range.

As is evident from the blue LI curve in **Figure 14**, the output power oscillates strongly as a function of current. Varying the injection current of the RSOA varies the temperature of the active region, which varies the refractive index through the thermo-

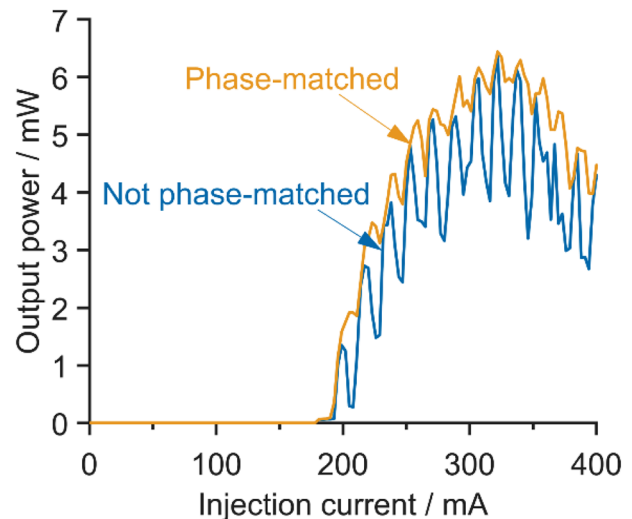


Figure 14. Measured IL curve of the hybrid laser at room temperature, without tuning the phase shifter (blue curve), and by tuning the phase shifter and maximizing the output power at each point (orange curve).

optic effect. This means that the phase of the RSOA changes as a function of injection current, while the phase of the Si₃N₄ circuit remains constant, which will lead to the oscillation between maximum and minimum phase-match between the RSOA and Si₃N₄ circuit, as was explained in Section 4.4. Thus, to phase-match the RSOA and Si₃N₄ circuit, current was injected into the phase shifter, and the LI curve was measured again, while maximizing the output power at each injection current value. The resulting LI curve is shown in orange in **Figure 14**. This time there is minimal oscillation, as expected, proving the effect of matching the phase of the RSOA and Si₃N₄ circuit by tuning the phase shifter.

A constant injection current of 325 mA, which is close to where the hybrid laser has its maximum output power, was injected to the RSOA, and the tuning range of the hybrid laser was measured by tuning one of the MRR heaters over one period, i.e., over 2π phase shift. The spectrum of the hybrid laser was

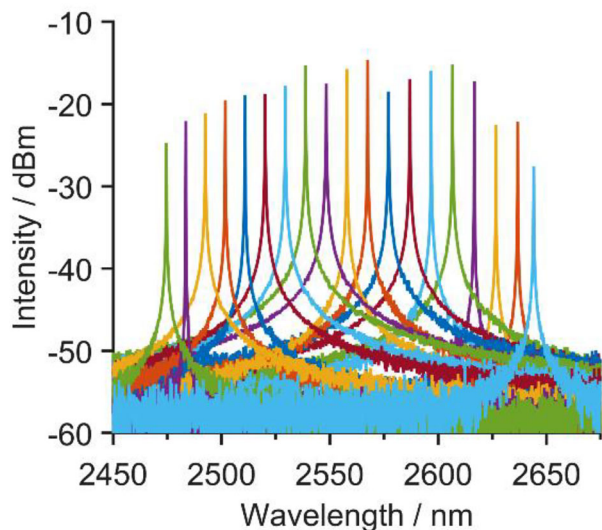


Figure 15. The spectrum of the hybrid laser measured at different MRR heater operation points at 325 mA injection current at room temperature.

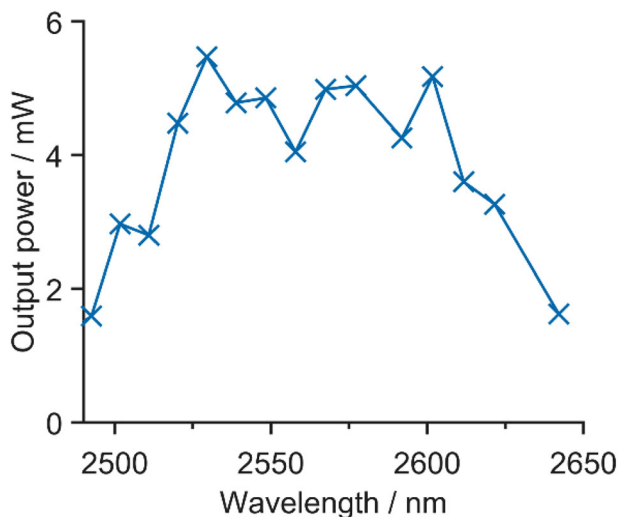


Figure 16. Output power of the hybrid laser as a function of wavelength at 325 mA injection current at room temperature.

measured with FTIR at several heater current values, and the result is shown in **Figure 15**. Looking at the measured spectra, the hybrid laser exhibits a very broad tuning range of ≈ 170 nm, with access to wavelengths between 2474 – 2644 nm. The 170 nm tuning range is relatively close to the simulated Vernier FSR of 160 nm. It is clear from the measured spectra that the hybrid laser is longitudinally single mode. The side-mode suppression ratio (SMSR) of the hybrid laser is 40 dB at the center of the tuning band and stays above 30 dB even at the edges of the band. The linewidth of the laser could not be measured accurately due to the limited resolution of the FTIR, as well as due to the noisy contacts of the probe needles with the MRR and phase shifters, leading to noise in the emission wavelength. Based on the measured FTIR spectra, the estimated linewidth is < 0.05 nm.

Next, a constant 325 mA of injection current was injected into the RSOA, and the hybrid laser was tuned to several wavelength points across the tuning range. The output power was maximized by tuning the phase shifter at each wavelength value. **Figure 16** shows the CW output power as a function of wavelength. The hybrid laser exhibits ≈ 5 mW of output power in the center of the tuning band (2520 nm – 2600 nm). Even at the edges of the tuning range, the power stays above 1 mW, which is more than enough for most sensing applications. The longest attainable wavelength is limited by the bandgap of the QWs, which explains the sudden drop in power at long wavelengths, while the low output power at the shorter wavelengths can be explained by lower gain, as well as the higher Vernier loss due to smaller coupling constant in the MRRs.

Table 1 shows a comparison of the performance of the hybrid laser presented in this work to the performance of other tunable hybrid lasers in the 1.9–3.0 μm wavelength region. Besides demonstrating the widest tuning range, the performance in terms of power and SMSR compares favorably with other GaSb-based hybrid lasers^[12,26,28] demonstrated earlier and is in general significantly superior to InP-based hybrid lasers^[13] where the emission wavelength is limited to < 2.4 μm .

6. Conclusion

In conclusion, we have demonstrated for the first time a Si_3N_4 -GaSb hybrid laser at 2.6 μm wavelength region, which utilizes the Vernier effect between two thermally tunable MRRs as the wavelength filtering and tuning mechanism. The hybrid laser exhibited a maximum CW output power of 6.4 mW at 322 mA and an extraordinarily broad tuning range of 170 nm, with an access to wavelengths between 2474 nm – 2644 nm. This is the highest CW output power beyond 2.1 μm ^[12] and the broadest tuning range beyond 1.7 μm ^[20] that has ever been reported for PIC-based tunable lasers. The operation voltage of the hybrid laser is 1.7 V at 300 mA injection current, demonstrating the suitability of the GaSb-based integration platform for applications where low power consumption is important, such as wearable sensors.

The performance of the building blocks can be further improved, e.g., by utilizing MM waveguides to achieve lower propagation losses, as well as improving the coupling efficiency by using the optimum taper width given by the simulations and optimizing the waveguide structure of the RSOA so that it matches better with the input Si_3N_4 waveguide mode. With lower losses, we expect that the performance of the hybrid laser will be significantly enhanced in terms of threshold current, output power, and spectral purity. The threshold current of the hybrid laser could also be lowered by increasing the reflectance of the rear facet of the RSOA, instead of leaving it as cleaved. The threshold of the hybrid laser could potentially also be reduced by implementing more QW layers in the epitaxial structure to increase the gain. However, more QW layers will also increase strain, as well as make the carrier distribution more nonuniform, which may lead to higher losses in the cavity.^[38] The tuning range of the hybrid laser could be made wider by designing a double-ring resonator with a wider FSR. Wider tuning range would also require lower overall losses, or alternatively a higher gain or broader gain

Table 1. Performance comparison with other tunable hybrid lasers in the 1.9–3.0 μm wavelength region.

| Laser type | Integration method | Wavelength (tuning range) [nm] | Maximum output power [mW] | SMSR [dB] |
|--|---------------------------|--|--|-----------|
| GaSb/SOI ^[28] | Hybrid integration | CW: 1983–1990 (7) | CW: 6.12 @ 23 °C | 32–37 |
| GaSb/SOI ^[12] | Hybrid integration | CW: 2011–2069 (58) | CW: 7.5 (uncooled) | >40 |
| InP/SOI ^[13] | Heterogeneous integration | Pulsed: 2325–2375 (50) CW: 2337–2362 (25) | Pulsed: 1 @ 25 °C CW: 0.4 @ 10 °C | >40 |
| GaSb/SOI ^[26] | Hybrid integration | Pulsed: 2550–2620 (70) | Pulsed: 10 @ 20 °C | 14 |
| This work, GaSb/Si ₃ N ₄ | Hybrid integration | CW: 2474–2644 (170) | CW: 6.4 @ 23 °C | 30–40 |

bandwidth for the RSOA. Higher gain could be achieved by utilizing more QW layers to increase the gain overall,^[39] and the gain bandwidth could be broadened by utilizing QW layers of different compositions or different thicknesses.^[40] Finally, with improved losses we should be able to tackle operation near 3.4–3.5 μm where Auger losses need to be balanced by reducing other types of losses.

7. Experimental Section

Simulation and Numerical Methods: The Si₃N₄ waveguide propagation loss simulations were performed utilizing Ansys Lumerical FDE, by varying the waveguide width and calculating the propagation loss for different waveguide widths at different wavelengths. The imaginary refractive index values of SiO₂ were taken from literature.^[15]

The heater simulations were performed utilizing COMSOL Multiphysics' Heat Transfer in Solids package. A heater layer was placed above the Si₃N₄ waveguide and was set as a heat source. The bottom plane of the PIC was set at 296 K temperature. A stationary simulation was then performed to find the equilibrium temperature of the Si₃N₄ waveguide.

The inverse taper simulation was performed utilizing Ansys Lumerical FDTD. Fundamental TE mode was excited at the RSOA waveguide, and the transmission to the fundamental TE mode of the Si₃N₄ waveguide mode was calculated at different taper input width and air gap values.

The inverse design of the Y-branch was performed utilizing Ansys Lumerical Photonic Inverse Design. An Ansys Lumerical FDTD simulation was set up, consisting of a 1.65 μm \times 0.8 μm input waveguide, which was coupled into the Y-branch structure, which then couples light into two 1.65 μm \times 0.8 μm output waveguides. The Y-branch was set to be symmetric along the x-axis, meaning that equal amount of light was coupled into the output waveguides. The Y-branch structure was defined as a symmetric polygon with 20 nodes on the outer surface whose y-coordinates determine the shape of the Y-branch. The y-coordinates of the nodes, i.e., the shape of the Y-branch, were optimized by performing Parametric Optimization with Ansys Lumerical Automation API, by maximizing the transmission of the Y-branch. A rectangular Y-branch was used as an initial guess in the optimization.

The transmission of the double-ring resonator was simulated utilizing Ansys Lumerical INTERCONNECT, where the individual building blocks of the circuit were simulated with Ansys Lumerical FDTD.

The cavity mode simulations were performed by solving Equation (4) utilizing MATLAB, where the phase-shift induced by the external part of the cavity was obtained by performing circuit simulations with Ansys Lumerical INTERCONNECT.

Experimental Methods: All the measurements were performed by placing the RSOA on an AlN submount on a heatsink that was stabilized to 23 °C with Keithley 2510 TEC Source Meter. The rear facet output of the RSOA was coupled to a Thorlabs ZrF₄ multimode fiber, and the output of the fiber was coupled to a VIGO PVI-4TE-4 photodetector. A SR540 optical chopper was placed between the optical fiber and the photodetector, and the chopping frequency was set to 300 Hz. The signal magnitude of the

photodetector was measured with a SR810 Lock In Amplifier, utilizing the trigger signal from the optical chopper.

To form the hybrid laser cavity, the Si₃N₄ PIC was placed on a custom vacuum holder, which was attached to a Thorlabs 3-Axis NanoMax closed-loop piezo stage. The piezo stage was controlled with Thorlabs KPZ101 Piezo Controllers and KSG101 Strain Gauge Readers. The coupling gap between the RSOA and PIC was manually adjusted with differential adjusters, and the y and z position was optimized by doing a 2D raster scan using the piezo controllers, and finding the position, which gave the maximum signal according to the lock in amplifier.

The power was calibrated by measuring the power of a known device with an integrating sphere: the device output was coupled to a Newport 819C Gold Collimated Beam Integrating Sphere, and the VIGO PVI-4TE-4 photodetector was placed at one of the outputs. The ASE output power of the rear facet of the RSOA was then measured with the same setup. Knowing the ASE output power of the rear facet of the RSOA then enables one to calculate the output power of the hybrid laser.

To tune the heaters on the PIC, needle probes were placed on the heater pads, and current was driven to the heaters utilizing Keithley 2604B Source Measure Unit. The IL measurement was performed by scanning the phase shifter from 0 to 40 V at each current value injected to the RSOA and recording the signal level with the lock in amplifier at each voltage. The “Not phase-matched” points in Figure 14 correspond to signal values recorded when 0 V voltage was applied to the phase shifter, while the “Phase-matched” points correspond to the maximum signal value recorded at each current value injected to the RSOA.

The spectrum of the hybrid laser was measured with a Bristol Instruments 771B Laser Spectrum Analyzer. The tuning spectra were recorded by applying constant 325 mA injection current to the RSOA and applying 0 V to 40 V voltage to the heater attached to one of the ring resonators, and measuring the spectrum at each voltage value. The output power at each wavelength value was obtained by applying 0 to 40 V voltage to the phase shifter and finding the voltage that leads to the maximum signal value.

Acknowledgements

The research was funded by EU Business Finland projects RAPS1 (decision 1613/31/2018) and PICAP (decision 44761/31/2020), as well as Vaisala Oyj. This work was part of Academy of Finland flagship program PREIN (decision 320168). S.-P.O. would like to thank Vaisala Oyj for the funding of the Ph.D. program. The authors wish to thank D.Sc. Heikki Virtanen for preparation of AR coatings.

Conflict of Interest

The authors declare no conflict of interest.

Data Availability Statement

The data that support the findings of this study are available from the corresponding author upon reasonable request.

Keywords

GaSb, silicon nitride photonics, photonic integrated circuits, laser diodes, tunable lasers, hybrid lasers, mid-infrared lasers

Received: December 29, 2022

Revised: March 31, 2023

Published online:

- [1] H. Debrégeas, F. Lelarge, S. Vankatesan, in *Proc. 23rd Eur. Conf. Integr. Opt.*, Milan, Italy, **2022**, pp. 279.
- [2] I. E. Gordon, L. S. Rothman, C. Hill, R. V. Kochanov, Y. Tan, P. F. Bernath, M. Birk, V. Boudon, A. Campargue, K. V. Chance, B. J. Drouin, J.-M. Flaud, R. R. Gamache, J. T. Hodges, D. Jacquemart, V. I. Perevalov, A. Perrin, K. P. Shine, M.-A. H. Smith, J. Tennyson, G. C. Toon, H. Tran, V. G. Tyuterev, A. Barbe, A. G. Császár, V. M. Devi, T. Furtenbacher, J. J. Harrison, J.-M. Hartmann, A. Jolly, et al., *J. Quant. Spectrosc. Radiat. Transf.* **2017**, *203*, 3.
- [3] A. K. Amerov, J. Chen, M. A. Arnold, *Appl. Spectrosc.* **2004**, *58*, 1195.
- [4] P. T. Lin, H. G. Lin, Z. Han, T. Jin, R. Millender, L. C. Kimerling, A. Agarwal, *Adv. Opt. Mater.* **2016**, *4*, 1755.
- [5] G. Yurtsever, B. Považay, A. Alex, B. Zabihian, W. Drexler, R. Baets, *Biomed. Opt. Express* **2014**, *5*, 1050.
- [6] D. Martens, A. Z. Subramanian, S. Pathak, M. Vanslebrouck, P. Binestman, W. Bogaerts, R. G. Baets, *IEEE Photonics Technol. Lett.* **2015**, *27*, 137.
- [7] D. Kohler, G. Schindler, L. Hahn, J. Milvich, A. Hofmann, K. Länge, W. Freude, C. Koos, *Light: Sci. Appl.* **2021**, *10*, 64.
- [8] F. Ghasemi, A. A. Eftekhar, D. S. Gottfried, X. Song, R. D. Cummings, A. Adibi, in *Self-Referenced Silicon Nitride Array Microring Biosensor for Toxin Detection Using Glycans at Visible Wavelength* (Eds.: A. N. Cartwright, D. V. Nicolau) SPIE, San Francisco, California, USA, **2013**, p. 85940A.
- [9] P. Munoz, P. W. L. van Dijk, D. Geuzebroek, M. Geiselmann, C. Dominguez, A. Stassen, J. D. Domenech, M. Zervas, A. Leinse, C. G. H. Roeloffzen, B. Gargallo, R. Banos, J. Fernandez, G. M. Cabanes, L. A. Bru, D. Pastor, *IEEE J. Sel. Top. Quantum Electron.* **2019**, *25*, 8200513.
- [10] K. Luke, Y. Okawachi, M. R. E. Lamont, A. L. Gaeta, M. Lipson, *Opt. Lett.* **2015**, *40*, 4823.
- [11] S. Sharma, S. Roy, *J. Supercomput.* **2021**, *77*, 4332.
- [12] R. Wang, A. Malik, I. Šimonytė, A. Vizbaras, K. Vizbaras, G. Roelkens, *Opt. Express* **2016**, *24*, 28977.
- [13] R. Wang, S. Sprengel, A. Vasiliev, G. Boehm, J. Van Campenhout, G. Lepage, P. Verheyen, R. Baets, M.-C. Amann, G. Roelkens, *Photonics Res.* **2018**, *6*, 858.
- [14] R. Wang, S. Sprengel, G. Boehm, R. Baets, M.-C. Amann, G. Roelkens, *Optica* **2017**, *4*, 92.
- [15] R. Kitamura, L. Pilon, M. Jonasz, *Appl. Opt.* **2007**, *46*, 8118.
- [16] T. Aalto, M. Cherchi, M. Harjanne, S. Bhat, P. Heimala, F. Sun, M. Kapulainen, T. Hassinen, T. Vehmas, *IEEE J. Sel. Top. Quantum Electron.* **2019**, *25*, 8201109.
- [17] M. Nedeljkovic, J. S. Penades, V. Mittal, G. S. Murugan, A. Z. Khokhar, C. Littlejohns, L. G. Carpenter, C. B. E. Gawith, J. S. Wilkinson, G. Z. Mashanovich, *Opt. Express* **2017**, *25*, 27431.
- [18] A. Sánchez-Postigo, J. G. Wangüemert-Pérez, J. Soler Penadés, A. Ortega-Moñux, M. Nedeljkovic, R. Halir, F. El Mokhtari Mimun, Y. Xu Cheng, Z. Qu, A. Z. Khokhar, A. Osman, W. Cao, C. G. Littlejohns, P. Cheben, G. Z. Mashanovich, Í. Molina-Fernández, *IET Optoelectron.* **2019**, *13*, 55.
- [19] A. Arbabi, L. L. Goddard, *Opt. Lett.* **2013**, *38*, 3878.
- [20] Y. Guo, X. Li, M. Jin, L. Lu, J. Xie, J. Chen, L. Zhou, *APL Photonics* **2022**, *7*, 066101.
- [21] C. Op de Beek, B. Haq, L. Elsinger, A. Gocalinska, E. Pelucchi, B. Corbett, G. Roelkens, B. Kuyken, *Optica* **2020**, *7*, 386.
- [22] C. Xiang, J. Liu, J. Guo, L. Chang, R. N. Wang, W. Weng, J. Peters, W. Xie, Z. Zhang, J. Riemensberger, J. Selvidge, T. J. Kippenberg, J. E. Bowers, *Science* **2021**, *373*, 99.
- [23] Y. Guo, R. Zhao, G. Zhou, L. Lu, A. Stroganov, M. Nisar, J. Chen, L. Zhou, *IEEE Photonics J.* **2021**, *13*, 1500813.
- [24] K. Vizbaras, M.-C. Amann, *Semicond. Sci. Technol.* **2012**, *27*, 032001.
- [25] X. Li, J. X. B. Sia, W. Wang, Z. Qiao, X. Guo, G. I. Ng, Y. Zhang, Z. Niu, C. Tong, H. Wang, C. Liu, *Optica* **2021**, *8*, 855.
- [26] S.-P. Ojanen, J. Viheriälä, M. Cherchi, N. Zia, E. Koivusalo, P. Karioja, M. Guina, *Appl. Phys. Lett.* **2020**, *116*, 081105.
- [27] M. Geiselmann, in *Integr. Opt. Devices Mater. Technol. XXV* (Eds: S. M. García-Blanco, P. Cheben), SPIE, United States, **2021**, p. 10.
- [28] N. Zia, H. Tuorila, J. Viheriälä, S.-P. Ojanen, E. Koivusalo, J. Hilska, M. Guina, *Opt. Express* **2022**, *30*, 24995.
- [29] M. Wormington, C. Panaccione, K. M. Matney, D. K. Bowen, *Philos. Trans. R. Soc., A* **1999**, *357*, 2827.
- [30] M. Cherchi, S. Ylinen, M. Harjanne, M. Kapulainen, T. Aalto, *Opt. Express* **2013**, *21*, 17814.
- [31] Kuan Pei Yap, A. Delage, J. Lapointe, B. Lamontagne, J. H. Schmid, P. Waldron, B. A. Syrett, S. Janz, *J. Lightwave Technol.* **2009**, *27*, 3999.
- [32] Y. Xu, P. Maier, M. Blaicher, P.-I. Dietrich, P. Marin-Palomo, W. Hartmann, Y. Bao, H. Peng, M. R. Billah, S. Singer, U. Troppenz, M. Moehrle, S. Randel, W. Freude, C. Koos, *Sci. Rep.* **2021**, *11*, 16426.
- [33] P.-I. Dietrich, M. Blaicher, I. Reuter, M. Billah, T. Hoose, A. Hofmann, C. Caer, R. Dangel, B. Offrein, U. Troppenz, M. Moehrle, W. Freude, C. Koos, *Nat. Photonics* **2018**, *12*, 241.
- [34] C. M. Lalau-Keraly, S. Bhargava, O. D. Miller, E. Yablonovitch, *Opt. Express* **2013**, *21*, 21693.
- [35] D. G. Rabus, *Integrated Ring Resonators*, Springer, Berlin Heidelberg **2007**.
- [36] K. Oda, N. Takato, H. Toba, *J. Lightwave Technol.* **1991**, *9*, 728.
- [37] L. A. Coldren, S. W. Corzine, M. L. Mašanović, *Diode Lasers and Photonic Integrated Circuits: Coldren/Diode Lasers 2E*, John Wiley & Sons, Inc., Hoboken, NJ, USA **2012**.
- [38] J. Piprek, P. Abraham, J. E. Bowers, *Appl. Phys. Lett.* **1999**, *74*, 489.
- [39] H. Yamazaki, A. Tomita, M. Yamaguchi, Y. Sasaki, *Appl. Phys. Lett.* **1997**, *71*, 767.
- [40] H. S. Gingrich, D. R. Chumney, S.-Z. Sun, S. D. Hersee, L. F. Lester, S. R. J. Brueck, *IEEE Photonics Technol. Lett.* **1997**, *9*, 155.